


Article

Study on the Anti-Photocorrosion Mechanism of Novel Self-Assembled Spherical Cu₂O/FePO₄ Z-Scheme Heterojunctions

Kuo Zhang ¹, Xiufei Zhao ¹, Hang Qian ¹, Lihong Chen ¹, Biyu Wu ¹, Xiao Yang ¹, Haonan Zou ¹, Yujiao Hu ¹, Feng Chen ², Borong Liao ¹, Hu Zhou ^{1,*}, Lei Zhang ³, Tianyi Ma ⁴ and Yusheng Zhang ^{1,*} 

¹ Key Laboratory of Theoretical Organic Chemistry and Functional Molecule (MoE), College of Chemistry and Chemical Engineering, Hunan University of Science and Technology, Xiangtan 411201, China; 22010602009@mail.hnust.edu.cn (K.Z.); zhaoxiufei@hnust.edu.cn (X.Z.); 20242108016@stu.kust.edu.cn (H.Q.); 22010602012@mail.hnust.edu.cn (L.C.); wubiyu@mail.hnust.edu.cn (B.W.); 24020601004@mail.hnust.edu.cn (X.Y.); 24010602002@mail.hnust.edu.cn (H.Z.); 2206080322@mail.hnust.edu.cn (Y.H.); 22010601019@mail.hnust.edu.cn (B.L.)

² Laboratory and Information Technology Center, Ningbo University of Finance and Economics, Ningbo 315175, China; chenfeng@nbufe.edu.cn

³ School of Resource & Environment and Safety Engineering, Hunan University of Science and Technology, Xiangtan 411201, China; s12222002@hnu.edu.cn

⁴ School of Science, RMIT University, Melbourne, VIC 3000, Australia; tianyi.ma@rmit.edu.au

* Correspondence: zhouhu@hnust.edu.cn (H.Z.); yushengzhang@hnust.edu.cn (Y.Z.)

Abstract: Cu₂O, a narrow-bandgap semiconductor with visible light absorption capabilities, faces limitations in photocatalytic applications due to photocorrosion from hole self-oxidation and insufficient light absorption. In this work, a series of novel spherical Cu₂O/FePO₄ Z-scheme heterojunctions were successfully synthesized via self-assembly to overcome these challenges. The photocurrent, electrical impedance spectroscopy (EIS), and photoluminescence (PL) tests showed that Cu₂O/1.5FePO₄ (CF1.5) had excellent electron hole separation efficiency. Subsequently, photocatalytic degradation was utilized as a probing technique to further confirm the above conclusions, with the kinetic reaction constants of CF1.5 being 2.46 and 11.23 times higher than those of Cu₂O and FePO₄, respectively. After five cycles of experiments and XPS analysis, it was found that the content of Cu(I) in CF1.5 did not significantly decrease after the reaction, indicating that it has superior anti-photocorrosion performance compared to single Cu₂O, which is also due to the establishment of a Z-scheme heterojunction. Systematic studies using radical scavenging experiments and ESR tests identified ·OH and ·O₂[−] as the main active species involved in photocatalysis. The formation of a Z-scheme heterojunction not only enhances the photocatalytic activity of the CF1.5 composite but also effectively suppresses the photocorrosion of Cu₂O, thereby offering a promising approach for enhancing anti-photocorrosion of Cu₂O.

Keywords: Cu₂O/FePO₄; Z-scheme heterojunction; photocatalytic degradation; anti-photocorrosion



Academic Editor: Lluís Soler

Received: 15 February 2025

Revised: 21 March 2025

Accepted: 27 March 2025

Published: 7 April 2025

Citation: Zhang, K.; Zhao, X.; Qian, H.; Chen, L.; Wu, B.; Yang, X.; Zou, H.; Hu, Y.; Chen, F.; Liao, B.; et al. Study on the Anti-Photocorrosion Mechanism of Novel Self-Assembled Spherical Cu₂O/FePO₄ Z-Scheme Heterojunctions. *Reactions* **2025**, *6*, 24. <https://doi.org/10.3390/reactions6020024>

Copyright: © 2025 by the authors. Licensee MDPI, Basel, Switzerland. This article is an open access article distributed under the terms and conditions of the Creative Commons Attribution (CC BY) license (<https://creativecommons.org/licenses/by/4.0/>).

1. Introduction

In recent years, photocatalysis has emerged as an environmentally friendly, efficient, and sustainable technology widely applied in carbon reduction, green energy conversion, and environmental management [1–3]. During the photocatalysis process, the generated active species such as ·OH, ·O₂[−], and h⁺, which are influenced by the semiconductor properties, can effectively be utilized for pollutant removal. Therefore, the development of efficient semiconductor photocatalysts is crucial for the practical application of photocatalysis technology [4,5]. Cu₂O, as a P-type narrow-band semiconductor with a direct bandgap

of 2.0–2.2 eV, is highly regarded by researchers and has been widely studied for its green, cheap, and easy availability [6]. Zhang et al. synthesized bifunctional Cu_2O materials for the degradation of methyl orange dye [7]. Nwanya et al. developed cubic crystalline Cu_2O nanoparticles for industrial textile wastewater treatment and antimicrobial applications [8]. Although it exhibited UV–visible light absorption, photoexcited holes that could not be compensated by electrons could oxidize Cu(I) to the low-photocatalytic-activity product Cu(II), resulting in so-called photocorrosion [9–11]. Hence, the primary challenge in enhancing the anti-photocorrosion of Cu_2O lies in facilitating the efficient separation of photogenerated electron–hole pairs to maximize solar energy utilization.

Hole oxidation is considered as the primary cause of highly active Cu(I) photocorrosion. The following methods could accelerate the transfer and migration of these holes: doping [12–17], crystal plane engineering [18–20], morphology control [21–24], and the construction of heterojunctions [25–27]. Interestingly, the construction of heterojunctions effectively facilitated the separation of electron–hole pairs, thereby achieving higher photocatalytic efficiency. Yu et al. successfully synthesized p-n $\text{Cu}_2\text{O}/\text{CaWO}_4$ heterojunction composite materials for the photocatalytic degradation of tetracycline and doxycycline [26]. The built-in electric field generated within the composite accelerated the transfer of electrons and holes at the interface, exhibiting superior photocatalytic activity compared to the individual components. However, the degradation rate of tetracycline decreased from 91.0% to 70.0% after five cycles, indicating poor cyclic stability. Ke et al. synthesized p-n $\text{Cu}_2\text{O}/\text{Bi}_2\text{O}_3$ heterojunction composites for water oxidation and MB dye degradation [27]. The composites suppressed the recombination of electron–hole pairs by enhancing charge separation, thereby enabling a higher number of photogenerated electrons and holes to participate in the oxidation of water molecules and dyes. However, after four cycles, the oxygen yield of the composite catalyst decreased to 74% of that of the fresh catalyst. Therefore, the constructed p-n heterojunction structure did not effectively address the photocorrosion issue of Cu_2O . Surprisingly, the Z-scheme heterojunction addressed these limitations by both accelerating the effective separation of electron–hole pairs and enhancing the anti-photocorrosion and stability of Cu_2O [28,29]. Sun et al. successfully synthesized a novel Z-type $\text{Cu}_2\text{ZnSnS}_4/\text{Cu}_2\text{O}$ (CZTS/ Cu_2O) photocatalytic composite using the solvothermal method and oxidation–reduction method. Due to the formation of heterojunctions, high charge carrier separation was presented, thus achieving excellent photocatalytic hydrogen production efficiency [28]. Bi et al. successfully synthesized a concave cubic Z-type $\text{ZnIn}_2\text{S}_4/\text{Cu}_2\text{O}$ heterojunction photocatalytic material with excellent light-driven CO_2 reduction performance by selective etching [29]. However, there is little other research. Therefore, it is crucial to find a material that forms a Z-scheme heterojunction with Cu_2O .

Iron phosphate (FePO_4), known as an N-type semiconductor, has been widely used in lithium-ion battery production because of its high photoactivity, excellent thermal stability, low cost, and easy recoverability. For example, Zhang et al.'s multi-component $\text{Cu}_2\text{O}@\text{FePO}_4$ core–cage structure has a fast electron transfer rate, which can realize highly sensitive in situ detection of nitric oxide [30]. However, FePO_4 has received limited attention as a photocatalyst. Researchers explored its application in photocatalysis and found that it exhibited excellent light absorption, electrical conductivity, and reusability [31,32]. However, the photocatalytic activity of pure FePO_4 is inhibited by the rapid recombination of its wide bandgap and charge carrier [33,34]. Beshkar et al. successfully prepared a CuI/FePO_4 p-n heterojunction photocatalyst for the degradation of amoxicillin, which exhibited no significant decrease in degradation rate after five cycles of testing [35]. Then, Tuo et al. successfully synthesized a $\text{FePO}_4/\text{g-C}_3\text{N}_4$ composite material, which maintained a consistent degradation rate of Rhodamine B (RhB) after five cycles of testing, demon-

strating the composite material's excellent cyclic stability [36]. Based on these studies, we attempted to construct a novel $\text{Cu}_2\text{O}/\text{FePO}_4$ Z-scheme heterojunction composite to achieve anti-photocorrosion and high photocatalytic activity.

In this paper, novel sphere $\text{Cu}_2\text{O}/\text{FePO}_4$ heterojunction photocatalytic composites were successfully synthesized by introducing FePO_4 into Cu_2O nanocubes using the self-assembly method. The Z-scheme heterostructure between Cu_2O and FePO_4 has been proved by a series of characterization methods. This discovery provides valuable insights, demonstrating that the synthesized $\text{Cu}_2\text{O}/\text{FePO}_4$ composite not only enhanced photocatalytic activity for the treatment of wastewater and electron hole separation efficiency but also effectively inhibited the photocorrosion of Cu_2O .

2. Materials and Methods

2.1. Material and Reagent

Anhydrous cupric acetate ($\text{Cu}(\text{CH}_3\text{COO})_2$, AR, 98.0%), sodium hydroxide (NaOH, AR, 95%), disodium hydrogen phosphate (Na_2HPO_4 , AR, 99.99%), Iron(III)nitrate nonahydrate ($\text{Fe}(\text{NO}_3)_3 \cdot 9\text{H}_2\text{O}$, AR, 99.99%), absolute ethanol ($\text{C}_2\text{H}_5\text{OH}$), methylene blue (MB, AR, $\geq 98.0\%$), 4-OH-TEMPO (AR, 98%), EDTA-2Na (AR, $\geq 99.0\%$), and IPA (AR, $\geq 99.7\%$) were the analytical reagents and were purchased from Aladdin (Shanghai, China) and Macklin (Shanghai, China). The absolute ethanol (AR, $\geq 99.7\%$) and distilled water (DW, 99.0%) can be used directly without any further purification.

2.2. Synthesis of the Samples

2.2.1. Synthesis of the Raw Cu_2O

The original Cu_2O was synthesized using the simple precipitation–reduction method reported by Lou et al. [31]. The synthesis procedure proceeded as follows: $\text{Cu}(\text{CH}_3\text{COO})_2$ (0.01 mol) was dispersed in 80 mL of deionized water, and the resulting solution was heated to 70 °C. Subsequently, NaOH (0.02 mol) and glucose (0.005 mol) were sequentially added. The solution was then maintained at 70 °C for 1 h. Afterward, the precipitate was isolated via centrifugation and dried in a 60 °C oven for 12 h.

2.2.2. Synthesis of the $\text{Cu}_2\text{O}/\text{FePO}_4$ Composite

The $\text{Cu}_2\text{O}/\text{FePO}_4$ composites were prepared via a simple hydrothermal method. Cu_2O (0.01 mol) and $\text{Fe}(\text{NO}_3)_3 \cdot 9\text{H}_2\text{O}$ (0.01 mol) powders were dispersed in ethanol solution using ultrasound for 1 h (referred to as solution A). Simultaneously, Na_2HPO_4 (0.01 mol) powder was dissolved in 30 mL of water by stirring (referred to as solution B). Solution B was then added dropwise to solution A. After 10 min of stirring, the resulting mixture was transferred to a 100 mL Teflonlined autoclave and reacted at 120 °C for 6 h. Upon cooling to room temperature, the solution was filtered, and the residue was then dried in a 60 °C oven for 12 h. By varying the amount of FePO_4 , composites with different molar ratios of 1:0.5, 1:1, 1:1.5, and 1:2 were synthesized, which were denoted as CF0.5, CF, CF1.5, and CF2, respectively.

The synthesis procedure for FePO_4 mirrors that of the $\text{Cu}_2\text{O}/\text{FePO}_4$ composite described above, with the exclusion of Cu_2O from the process.

2.3. Characterization Techniques

The properties of the composites were characterized by various photocatalytic analysis techniques. The structure and phase composition of the composites were investigated by an X-ray diffractometer (XRD, X'Pert PRO MPD) running at a scan rate of 5°/min in the 2 θ range of 5–90° using Cu-k α monochromatic radiation (1.5406 Å, 45 KV, 40 mA). The surface morphology and structure of the prepared samples were characterized by scanning

electron microscopy (SEM) (Hitachi Regulus8100, Hitachi High-Tech Corporation, Tokyo, Japan). Prior to the experiment, gold spraying was performed to enhance the conductivity of the materials. Then, the elements of the composite were verified by energy dispersive X-ray spectroscopy (EDX). In addition, the valence states and molecular structures of elements on the surface of the composite were measured by X-ray photoelectron spectroscopy (XPS, Thermo Kalpha, ThermoFisher, Nashville, TN, USA), and the valence band spectra of the raw Cu_2O and FePO_4 were obtained. The optical properties of the monomers and composites were studied by a visible light diffuse reflection spectrophotometer (UV-vis DRS, PE lambda 750, PerkinElmer, Waltham, MA, USA) and photoluminescence fluorescence spectrophotometer (photoluminescence, Hitachi F-4500, Japan) with an excitation wavelength of 300 nm. The specific surface area (BET), pore volume, and pore size of the material were measured by physical adsorption apparatus (BSD-PS) at 200 °C for 6 h after degassing with nitrogen. The electrical impedance (EIS) and photocurrent of the photocatalytic material were measured using an electrochemical workstation. In this experiment, we used a three-electrode system for electrochemical testing. Pt was the opposite electrode, Ag/AgCl was the reference electrode, and the catalyst was the working electrode. Then, 5 mg of the catalyst was mixed with 20 μL of Nafion solution and sonicated to achieve complete dispersion. The dispersed solution was evenly dropped onto a rectangular FTO conductive glass using a pipette and then heated at 60 °C for 1 h in an oven. Finally, the FTO conductive glass loaded with the catalyst was placed on the working electrode side in a 0.1 M Na_2SO_4 solution for testing. The absorbance of methylene blue dye in different time periods was determined by UV-1800PC (AOELAB, Shanghai, China).

2.4. Photocatalytic Degradation Experiments

The photocatalytic performance was evaluated by the degradation of MB pollutants in a 300 W xenon lamp (CEL-HXF300) under visible light irradiation ($\lambda > 420 \text{ nm}$). For each experiment, before the light source was turned on the 20 mg $\text{Cu}_2\text{O}/\text{FePO}_4$ photocatalyst was dispersed into 50 mL of MB pollutants (20 mg/L). The mixture was stirred in the dark for 30 min to achieve adsorption–desorption equilibrium. During illumination, approximately 4 mL of the solution was sampled every 20 min, and the catalyst powder was removed using a 0.45 μm filter. The absorbance of the MB solution was measured at 665 nm using a UV–visible spectrophotometer. Since the absorbance and concentration were proportional in a certain range, the degradation rate of MB solution by the $\text{Cu}_2\text{O}/\text{FePO}_4$ photocatalyst was calculated with the absorbance value directly instead of the concentration value, which was calculated from Equation (1):

$$\eta(\%) = (\text{Abs}_0 - \text{Abs}_t) / \text{Abs}_0 \times 100\% \quad (1)$$

where Abs_0 is the initial absorbance value of the MB solution, and Abs_t is the MB absorbance value in a certain time period. Continuing from there, we conducted photocatalytic cycling experiments using 20 mg of catalyst to degrade a 50 mL solution of 20 mg/L MB. After each sampling, the catalyst powder was subjected to centrifugation, rinsing, reclamation, and then drying at 60 °C in an oven prior to commencing the subsequent experimental cycle. The active free radicals $\cdot\text{OH}$, $\cdot\text{O}_2^-$, and h^+ generated during the photocatalytic reaction play an important role in the degradation and reduction process. The main schemes of active free radicals were determined by radical trapping experiments. According to the evaluation of reaction activity, under neutral conditions, 100 μL isopropyl alcohol (IPA), 1 mmol EDTA-2Na, and 1 mmol 4-OH-TEMPO were added to the reaction system as trapping agents for $\cdot\text{OH}$, h^+ , and $\cdot\text{O}_2^-$ radicals, respectively.

3. Results and Discussion

3.1. Characterizations

Figure 1a illustrates the phase structure and crystallinity of the synthesized sample determined via X-ray powder diffraction (XRD). The major diffraction peaks of pure Cu_2O observed at 29.6° , 36.2° , 42.4° , 61.5° , and 73.7° correspond to the (110), (111), (200), (107), and (311) crystal planes of Cu_2O (JCPDS No. 77-0199), respectively. Additionally, the presence of the (102) crystal plane, characteristic of amorphous FePO_4 at 25.8° , conforms to the typical diffraction pattern of hexagonal FePO_4 (JCPDS No. 50-1635). The XRD pattern of the CF1.5 composite synthesized via the hydrothermal method exhibits obvious peaks attributable to both Cu_2O and FePO_4 . Particularly notable is the prominent diffraction peak at 25.8° corresponding to the (102) crystal plane of FePO_4 , indicating its presence within the composite. Furthermore, CF1.5 composites show the diffraction characteristic peaks of pure FePO_4 , which indicates that the crystal structure of FePO_4 can be improved and the heterostructure can be formed by a hydrothermal composite. Figure 1b presented the comprehensive measurement spectra of samples Cu_2O , FePO_4 , and CF1.5, clearly demonstrating the presence of Cu, O, Fe, and P elements.

SEM images of Cu_2O , FePO_4 , and CF1.5 are depicted in Figure 1c–f. As shown in Figure 1c, Cu_2O presented a microcube with a side length of about 500 nm. Figure 1d is the SEM image of FePO_4 nanoparticles with indefinite morphology, showing the morphology of massive accumulation. Figure 1e,f shows the CF1.5 composite synthesized via the self-assembly method, displaying a homogeneous and same-size spherical structure attributed to the interfacial deposition of FePO_4 on Cu_2O and the photoetching process of Cu_2O . This structural arrangement is corroborated by Zhang et al.'s study on $\text{Cu}_2\text{O}@ \text{FePO}_4$ CC synthesized using a template-assisted deposition method [30]. The spherical structure of the composite was homogeneous, with Cu_2O in close contact with FePO_4 , which facilitated the transfer and recombination of electron–hole pairs. According to the Supplementary Materials, specifically Figures S1 and S2, iron and phosphate ions exhibited a certain aggregation effect on Cu_2O but did not individually form spherical structures, nor did they exist in a homogeneous state. Simultaneously, the changes in the morphology of $\text{Cu}_2\text{O}/\text{FePO}_4$ composite materials with different ratios are illustrated in the SEM images shown in Figures S3–S5 of the Supplementary Materials. To further confirm the successful formation of the $\text{FePO}_4/\text{Cu}_2\text{O}$ composite, elemental mapping and energy-dispersive X-ray spectroscopy (EDX) analyses were performed on the CF1.5 sample, as shown in Figure 1g,h. The cubic structures on the surface of the spheres were primarily composed of Cu, with a uniform distribution of Cu, Fe, P, and O elements across the surface. The atomic percentage data provided in Supplementary Material Table S1 indicated that the mass fraction of Cu (21%) was lower than the standard value (34.4%). This discrepancy suggests several possibilities: (1) the presence of a certain amount of Cu_2O cubes on the sphere's surface rather than a homogeneous composite microsphere; (2) the influence of the selection range.

The photocatalytic performance of a photocatalyst is significantly influenced by its specific surface area and pore size. Table 1 presents the specific surface area, pore volume, and pore size of the synthesized samples. As indicated in the table, CF exhibits an increased specific surface area compared to the individual Cu_2O . This indicates that the CF composite spherical structure after self-assembly not only improves the specific surface area of the material, but also provides more adsorption sites, and the increase in specific surface area and active sites will improve the degradation efficiency of dyes to a certain extent.

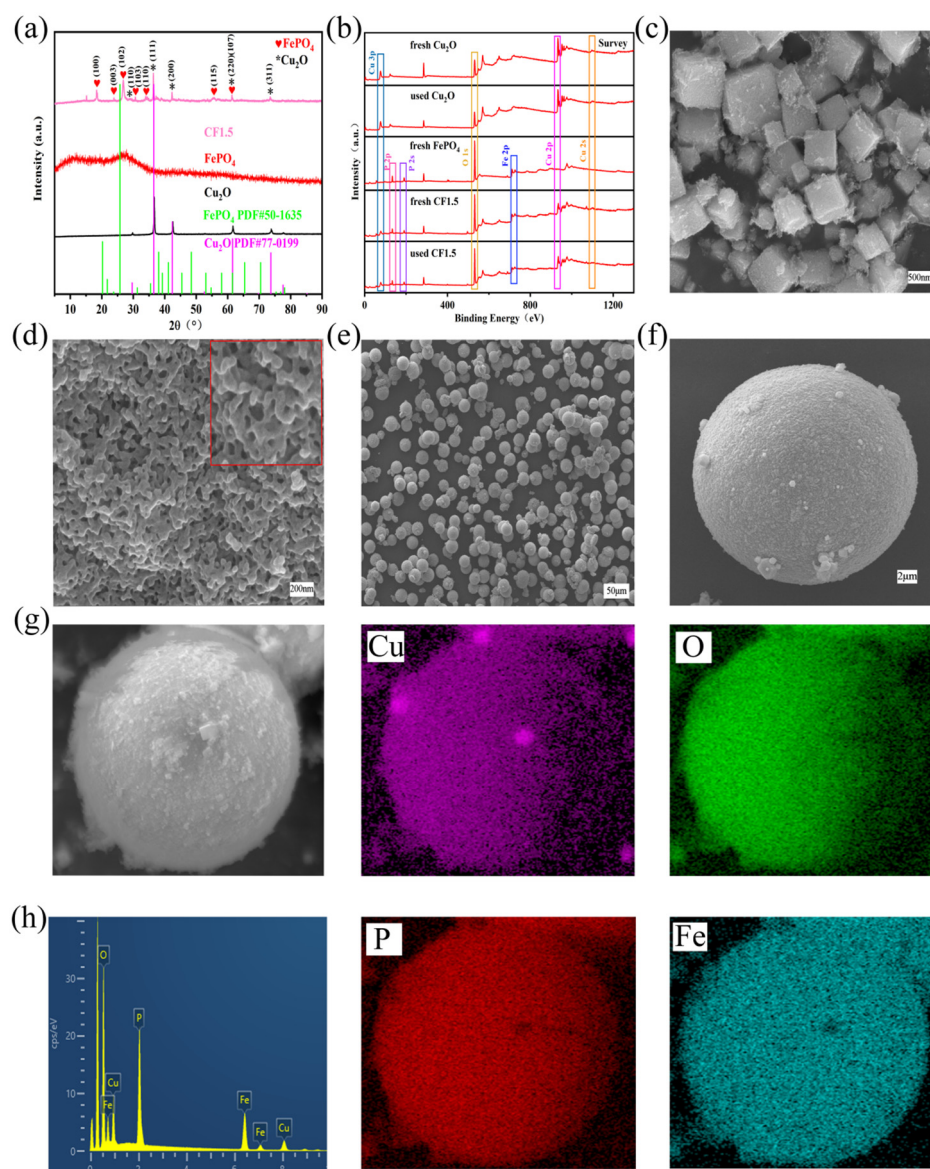


Figure 1. (a) XRD patterns and (b) XPS spectrum of as-prepared samples; SEM images of (c) Cu_2O , (d) FePO_4 , and (e,f) CF1.5; and (g) element mapping of and (h) EDX of CF1.5.

Table 1. The BET specific surface area, pore volume, and pore diameter of the as-prepared samples.

Samples	Specific Surface Area (m^2/g)	Pore Volume (mL/g)	Pore Diameter (nm)
Cu_2O	5.1826	0.0255	19.6812
FePO_4	70.4664	0.7064	40.0985
CF0.5	9.1060	0.0172	7.5555
CF	23.0821	0.0777	13.4650
CF1.5	17.3974	0.0348	8.0012
CF2	12.6882	0.0210	6.6203

The light absorption capacity of the Cu_2O , FePO_4 , and CF1.5 composites was evaluated by UV–vis diffuse reflectance spectroscopy (UV–vis DRS), and the corresponding Tauc plot was calculated by Equation (2):

$$\alpha h\nu = A(h\nu - E_g)^2 \quad (2)$$

where α , $h\nu$, and A are the absorption coefficient, photon energy, and energy-independent constants, respectively [37,38]. As shown in Figure 2a, FePO₄ showed the strongest absorption peak around 270 nm and a light absorption edge around 350 nm in the ultraviolet region, while Cu₂O showed a wider absorption peak in the entire ultraviolet region. The spherical structures formed after hydrothermal treatment exhibit larger sizes compared to the cubic Cu₂O and amorphous FePO₄ observed in the SEM images (Figure 1c–f). This enlargement is advantageous for enhancing the absorption of visible light.

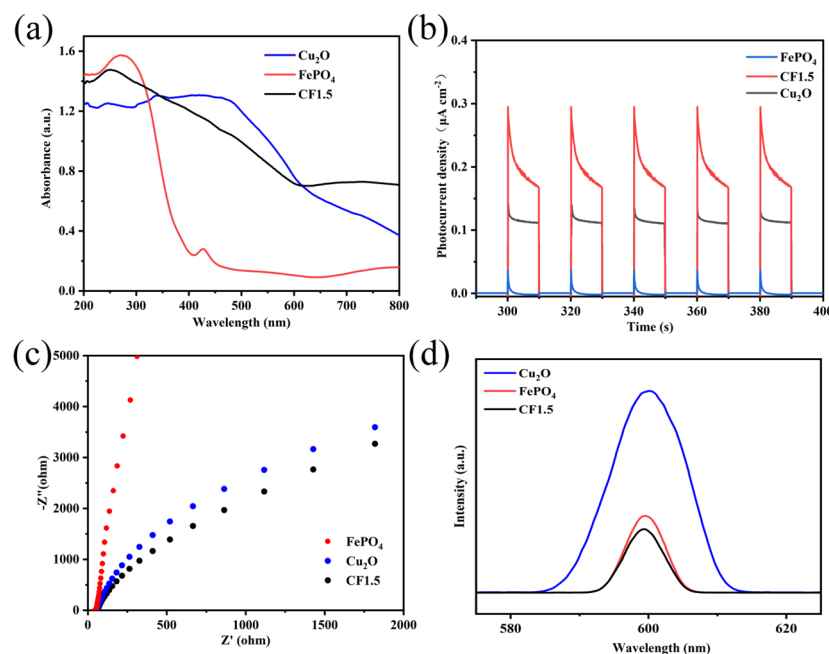


Figure 2. (a) UV–vis DRS spectra; (b) transient photocurrent responses; (c) EIS Nyquist plots; and (d) time-resolved transient photoluminescence (PL) decay curves of as-prepared Cu₂O, FePO₄, and CF1.5.

The generation efficiency of photogenerated electron–hole pairs was analyzed by controlling the transient photocurrent response under intermittent light conditions [39]. As depicted in Figure 2b, CF1.5 exhibited a higher photocurrent intensity and improved photocharge transfer efficiency compared to pure Cu₂O and FePO₄ during the repeated on–off cycling experiments with a 10 s interval. The low photocurrent response of FePO₄ and Cu₂O may be due to the rapid recombination of electron–hole pairs. Compared with Cu₂O and FePO₄, the photocurrent density of the CF1.5 heterojunction has been widely improved. These results indicate that FePO₄-modified Cu₂O microcubes promote the separation and transfer of photogenerated charge carriers, and inhibit the recombination of photogenerated electron–hole pairs. Additionally, the electrochemical impedance spectroscopy (EIS) results shown in Figure 2c were employed to assess the resistance associated with the photogenerated charge during the transfer process. The smaller the arc radius in the Nyquist plot, the lower the interfacial charge transfer resistance of the catalyst material, which facilitates the transfer of photogenerated electrons [40]. The arc radius of CF1.5 was notably smaller than that of the individual catalyst components, indicating reduced resistance for photogenerated electron migration. Consequently, the enhanced surface electron transfer efficiency of the CF1.5 composite not only boosted photocatalytic degradation performance but also mitigated the recombination of electron–hole pairs in Cu₂O, imparting the composite with certain anti-photocorrosion properties. Fluorescence measurements, shown in Figure 2d, were conducted on the samples under excitation at approximately 300 nm. CF1.5 displayed the weakest emission peak intensity compared

to Cu_2O and FePO_4 , suggesting a reduction in electron–hole pair recombination. Wang and colleagues' research indicated that the reason for this outcome is the formation of a heterojunction between the two individual substances [40].

Figure 3a–c present the photocatalytic activity and performance of pure Cu_2O , FePO_4 , and $\text{Cu}_2\text{O}/\text{FePO}_4$ composites for the visible light-induced degradation of MB solution. Controlled experiments demonstrated that the self-photolysis efficiency and adsorption rates of MB molecules on the photocatalyst are minimal (Figure 3a). As shown in Figure 3a, irradiation of pure Cu_2O and FePO_4 nanostructures under visible light for 2 h results in the removal of approximately 69% and 28% of the MB dye, respectively. The relatively low photolysis efficiency of Cu_2O and FePO_4 nanoparticles can be attributed to their low optical efficiency and a high rate of electron–hole pair recombination [31]. In contrast, the photocatalytic degradation efficiency of $\text{Cu}_2\text{O}/\text{FePO}_4$ composites with varying molar ratios surpasses that of the individual Cu_2O and FePO_4 catalysts, achieving a maximum degradation efficiency of 94% at a molar ratio of 1:1.5. Among all the samples, CF1.5 demonstrated the highest photocatalytic degradation efficiency for MB, with its kinetic constants being approximately 2.46 times and 11.23 times greater than those of pure Cu_2O and FePO_4 , respectively (Figure 3b). In addition to superior photocatalytic performance, the cyclic stability of the photocatalyst is crucial. The stability of Cu_2O and CF1.5 composites was evaluated through multiple cycles of MB degradation. Figure 3c illustrates that we conducted five cycles of photocatalytic degradation experiments on Cu_2O and CF1.5. The data reveal that the photocatalytic performance of CF1.5 remained largely stable, with degradation rates consistently above 92%. In contrast, pure Cu_2O showed a gradual decline in degradation efficiency, decreasing by approximately 5% per cycle, indicating substantial photocorrosion. In the Supplementary Material, Table S2 shows the work on MB degradation by Cu_2O -based photocatalysts in recent years. It can be seen that the CF1.5 photocatalyst used in this work has excellent stability. In order to explore the wide applicability of the CF1.5 photocatalyst for the treatment of water pollutants, a series of photodegradation and cycling experiments were conducted on tetracycline (TC) and Congo red (CR) solutions with the same concentration as MB, respectively (Figure 3d–f). The results showed that the photocatalyst not only had a high removal efficiency of water pollutants, but also had excellent cycling stability.

Subsequently, XPS analyses were conducted on fresh Cu_2O , used Cu_2O , fresh CF1.5, and used CF1.5 and FePO_4 samples (Figure 4a–d). As shown in Figure 4a, the XPS spectrum of Cu exhibits two peaks at 932.3 eV and 952.4 eV, corresponding to Cu^+ 2p_{3/2} and Cu^+ 2p_{1/2}, respectively [41]. The presence of Cu^{2+} primarily results from the oxidation of Cu_2O to CuO during the preparation process [42,43]. Two additional weak peaks for Cu^{2+} are observed at 934.3 eV and 955.0 eV for Cu 2p_{3/2} and Cu 2p_{1/2}, respectively [44]. The content of monovalent copper in used Cu_2O significantly decreases, while the divalent copper content increases, indicating substantial photocorrosion of Cu_2O . This change was attributed to the effective migration of valence electron density away from the Cu nucleus, resulting in reduced inner-shell electron shielding. Compared to the peak of Cu_2O before the reaction, the Cu 2p peak of Cu_2O after the reaction showed a noticeable blue shift [45]. Figure 4b clearly shows that the Cu^+ content in both fresh CF1.5 and used CF1.5 remains largely unchanged, further demonstrating the superior anti-photocorrosion capability of CF1.5. Compared to the Cu 2p_{1/2} peak of fresh CF1.5, the Cu 2p_{1/2} peak of used CF1.5 exhibits a red shift. Additionally, the rearrangement of outer-shell electrons in Cu has resulted in the appearance of three satellite peaks at 943.6 eV, 941.6 eV, and 962.2 eV in the Cu 2p spectrum [44]. As shown in Figure 4c, the Fe 2p band could be reverse-spun into four peaks of 711.6 eV, 718.1 eV, 724.9 eV and 732.7 eV, which belong to Fe 2p_{3/2}, the satellite peaks of Fe 2p_{3/2}, Fe 2p_{1/2} and the satellite peaks of Fe 2p_{1/2},

respectively. This confirmed the presence of Fe^{3+} in the material [46,47]. Increased electrical screening of the inner shell of Fe causes the Fe 2p peak of CF1.5 to redshift compared to pure Cu_2O . The O 1s spectrum in Figure 4d can be convolved into three sub-peaks, and the O1 peak at 532.1 eV corresponds to the hydroxyl group adsorbed on the surface [48]. Hydroxy-oxygen could not only improve the photocatalytic ability of the composite, but also promote the photocatalytic reaction. The O2 peak appearing at 531.09 eV was the formation of the P-O bond in PO_4^{3-} . The O3 peak at 529.7 eV was attributed to lattice oxygen (O_2) induced by O bonding with metals Cu and Fe [49,50]. It is well known that changes in electron binding energy are due to changes in the coulomb force between the nucleus and its outer electrons [51,52]. Compared with pure Cu_2O and pure FePO_4 , the binding energy of Cu, Fe, P, and O in CF1.5 moved in a lower or higher direction, which confirms the charge movement after Cu_2O and FePO_4 contact [53]. The wide peak shown in Figure S6 corresponds to the binding energy of P 2p associated with P(V) in PO_4^{3-} , which is consistent with the findings reported by Wu et al. [54]. The results from the cyclic experiments and XPS analyses provide robust evidence supporting the superior anti-photocorrosion properties of CF1.5 and the formation of the heterojunction.

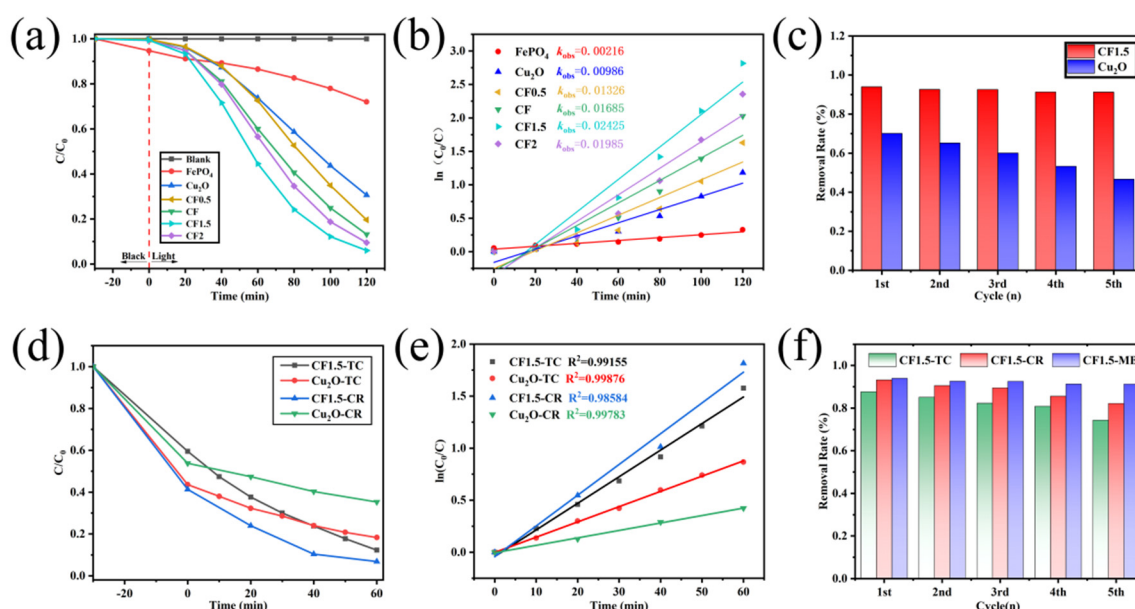


Figure 3. (a) Photodegradation of MB (50 mL, 20 mg/L) by different photocatalysts under visible light irradiation ($\lambda > 420$ nm); (b) kinetic linear simulation curves and (c) recycling performance experiments of Cu_2O and CF1.5; (d) photodegradation of TC and CR (50 mL, 20 mg/L) by CF1.5 and Cu_2O photocatalysts; (e) kinetic linear simulation curves; and (f) recycling performance experiments of CF1.5.

The direct bandgap width of pure Cu_2O and pure FePO_4 were measured by using Kubelka–Munk theory. As shown in Figure 5a, the bandgap energies of pure Cu_2O and pure FePO_4 were 1.86 eV and 2.85 eV, respectively, consistent with the results reported by Beshkar and Wang et al. [31,49]. Meanwhile, the $E_{\text{VB},\text{xps}}$ of Cu_2O and FePO_4 were -0.06 eV and 2.47 eV (Figure 5b) according to the XPS valence band spectrum, respectively. The valence bands of Cu_2O and FePO_4 can be calculated using Equation (3):

$$E_{\text{VB}} = \varphi + E_{\text{VB},\text{xps}} - 4.44 \quad (3)$$

where φ (4.2 eV) is the work function of the instrument and E_{VB} is the valence band position relative to the NHE. The E_{VB} of Cu_2O and FePO_4 is -0.3 eV and 2.23 eV, respectively. The E_{CB} values of Cu_2O and FePO_4 can be calculated by Equation (4):

$$E_g = E_{VB} - E_{CB} \quad (4)$$

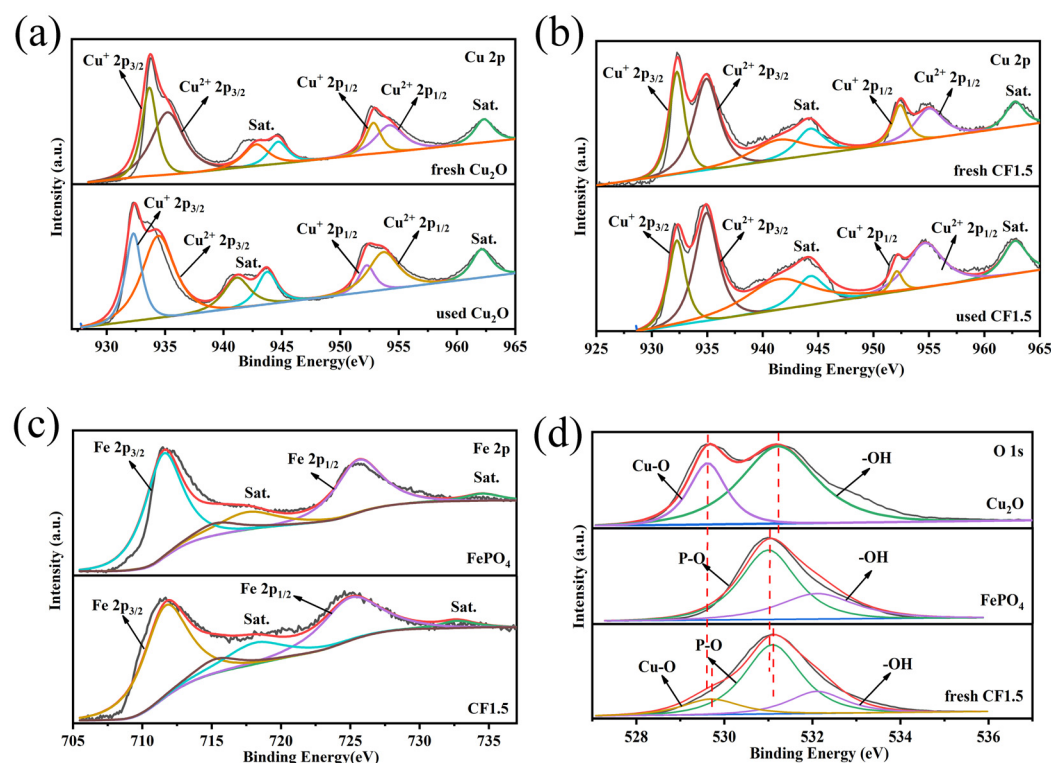


Figure 4. XPS analysis of as-prepared Cu_2O , FePO_4 , and CF1.5 of (a,b) Cu 2p, (c) Fe 2p, and (d) O 1s.

The band value (E_{VB}) is obtained by VB-XPS. The conduction band (E_{CB}) values for Cu_2O and FePO_4 are calculated to be -2.16 eV and -0.62 eV, respectively. To better visualize the electron band structure and compare the reduction and oxidation capacities of the conduction and valence bands, the relevant band spectra are presented in Figure 5c. The figure reveals that Cu_2O 's conduction band exhibits a strong negative potential, while FePO_4 's valence band shows a strong positive potential. This indicates that the E_{CB} of Cu_2O possesses good reducing ability, whereas the EVB of FePO_4 demonstrates strong oxidizing capability.

To further elucidate the degradation mechanism of the photocatalysts, we investigated the effects of active free radicals and substances produced on the surface of pure Cu_2O and $\text{Cu}_2\text{O}/\text{FePO}_4$ heterojunctions on MB degradation using free radical capture experiments and ESR spectroscopy. EDTA-2Na (1 mmol), 4-OH-TEMPO (1 mmol), and IPA (100 μL) were introduced to the photocatalytic reaction system as scavengers for h^+ , $\cdot\text{O}_2^-$, and $\cdot\text{OH}$, respectively. As shown in Figure 5d, in the Cu_2O system, compared to the solution without a scavenger (69.40%), the degradation rates of $\cdot\text{O}_2^-$, $\cdot\text{OH}$, and h^+ in the MB solution decreased by 56.01%, 7.48%, and 65.62%, respectively, upon addition of the scavenger. The addition of EDTA-2Na and 4-OH-TEMPO scavengers significantly decreased the photodegradation efficiency, indicating that h^+ and $\cdot\text{O}_2^-$ played the main active role in the degradation of MB solution by Cu_2O . In the CF1.5 system, compared to the solution without a scavenger (94.01%), the degradation rates of $\cdot\text{O}_2^-$, $\cdot\text{OH}$, and h^+ in the MB solution decreased by 57.76%, 23.29%, and 4.92%, respectively, upon addition of the scavenger. The addition of IPA and 4-OH-TEMPO scavengers significantly decreased the photodegradation efficiency, indicating that $\cdot\text{OH}$ and $\cdot\text{O}_2^-$ played a major role in the degradation of MB in CF1.5 solution. In order to verify the charge transfer mechanism of the CF1.5 heterojunction, the electron spin resonance (ESR) spectra of Cu_2O and CF1.5 were measured. Figure 5e–h

shows the ESR signal of DMPO conventional class capture radicals. In the absence of light exposure, the signal of DMPO- $\cdot\text{OH}$ and DMPO- O_2^- is basically invisible. This provided direct evidence for the construction of a CF1.5 Z-scheme heterojunction. The mechanism will be discussed in depth below.

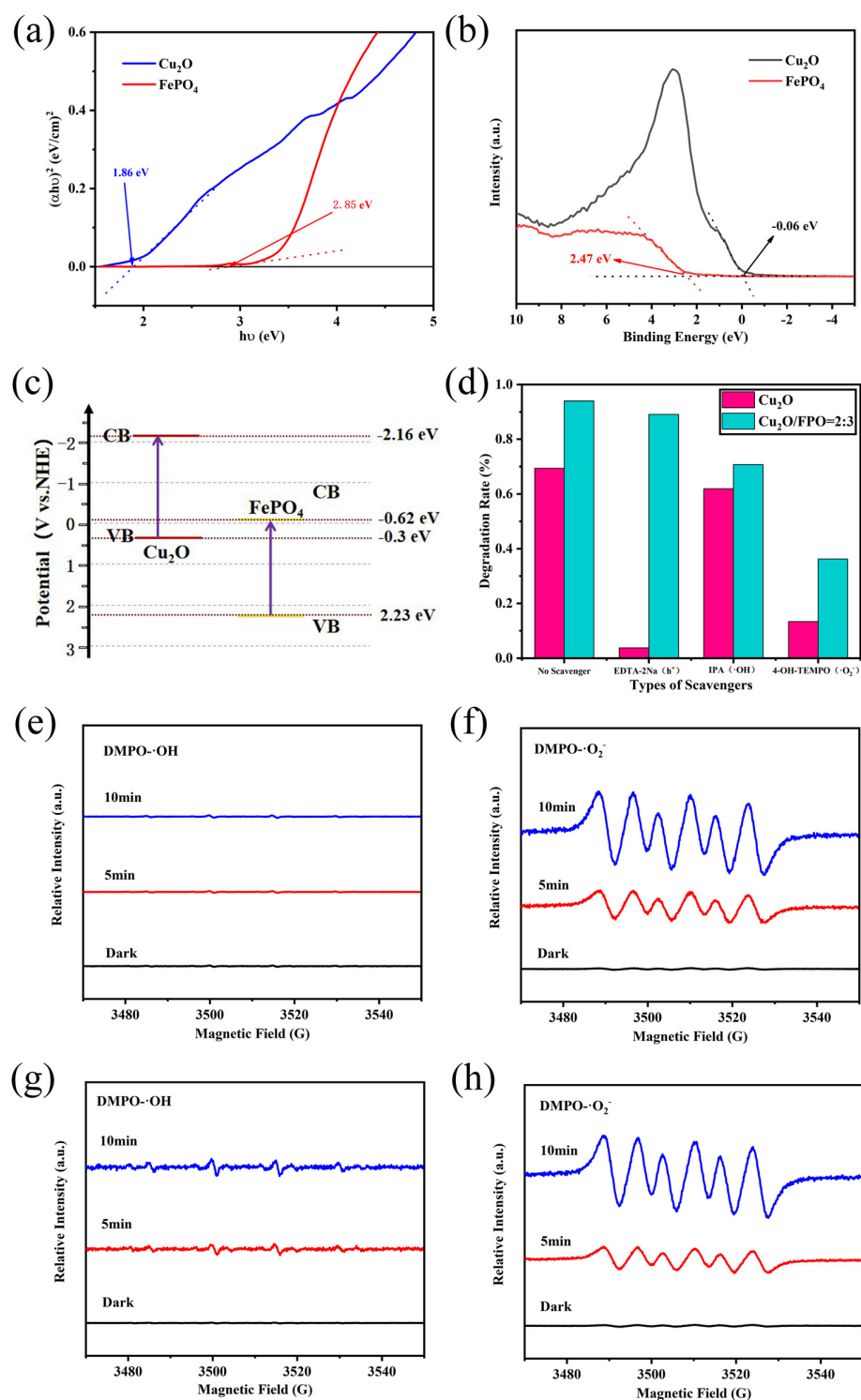


Figure 5. (a) Band energies of Cu_2O and FePO_4 determined by the Tauc plot; (b) VB-XPS spectra and (c) schematic illustration of the band structures of Cu_2O and FePO_4 ; (d) free radical trapping experiments of Cu_2O and CF1.5 under different scavengers; ESR signals of (e,f) DMPO- $\cdot\text{OH}$ and (g,h) DMPO- O_2^- adducts in the presence of Cu_2O and CF1.5 under visible light irradiation ($\lambda > 420 \text{ nm}$), respectively.

3.2. Photocatalytic Mechanism and Discussion

Based on the above result analysis, we propose a Z-scheme mechanism of MB degradation by $\text{Cu}_2\text{O}/\text{FePO}_4$ (Figure 6). In Figure 6a, the diagram illustrates the degradation mechanism of Cu_2O . According to the results of free radical capture experiments and ESR testing, it is known that the active species involved in the Cu_2O reaction are superoxide radicals ($\cdot\text{O}_2^-$) and holes (h^+). Cu_2O nanoparticles are excited by sunlight to produce photogenerated electrons and photogenerated holes. The optical excitation of electrons transfers them to the Cu_2O surface, where they then react with dissolved oxygen to generate super oxygen free radicals (O_2^-) [55]. On the other hand, photogenic holes can oxidize water or hydroxyl group (OH^-) adsorbed on the catalyst surface to form hydroxyl radicals ($\cdot\text{OH}$). These strongly oxidizing hydroxyl ($\cdot\text{OH}$) radicals, superoxide radicals ($\cdot\text{O}_2^-$), and holes (h^+) participate in the degradation process of dyes [56,57]. Figure 6b shows the photocatalytic mechanism of the $\text{Cu}_2\text{O}/\text{FePO}_4$ heterojunction after contact. The electrons in the Cu_2O and FePO_4 valence bands were stimulated by light and transferred to the conduction bands of Cu_2O and FePO_4 , leaving holes in their valence bands, respectively. Since the E_{CB} (-2.16 eV) of Cu_2O is more negative than that of $\text{O}_2/\cdot\text{O}_2^-$ (-0.33 eV vs. NHE), the e^- of the valence band of Cu_2O has a strong reducing ability. Similarly, h^+ in the valence band of FePO_4 was more positively charged than $\text{H}_2\text{O}/\cdot\text{OH}$ (1.99 eV vs. NHE), and its accumulation of photogenic holes in the valence band could effectively oxidize H_2O to $\cdot\text{OH}$. The active substance $\cdot\text{O}_2^-$ produced on the surface of Cu_2O could not only directly participate in the degradation of pollutants, but also combine with H^+ to produce H_2O_2 , and then decompose into $\cdot\text{OH}$, which acts on pollutants together with the $\cdot\text{OH}$ produced on the surface of FePO_4 . Compared to individual Cu_2O , where some of the holes participate in the degradation of pollutants while others can oxidize Cu_2O itself, in the $\text{Cu}_2\text{O}/\text{FePO}_4$ system, the band alignment between Cu_2O and FePO_4 enables the photogenerated holes in the valence band of Cu_2O to recombine with the photogenerated electrons transferred from the conduction band of FePO_4 . This process effectively prevents the self-oxidation of photogenerated holes in Cu_2O , thereby suppressing photocorrosion. Ultimately, this results in a Z-scheme heterojunction photocatalytic composite material with high stability and enhanced photocatalytic activity.

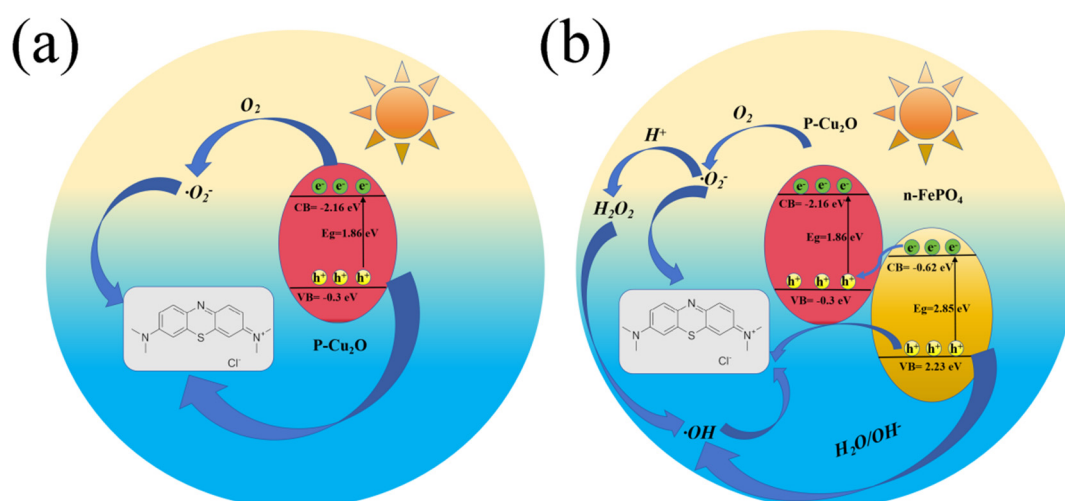


Figure 6. Schematic illustration of the degradation of MB by the as-prepared (a) Cu_2O ; (b) Z-scheme $\text{Cu}_2\text{O}/\text{FePO}_4$ heterojunction under visible light irradiation.

4. Conclusions

In this work, we synthesized a high-efficiency photocatalytic Z-scheme composite material $\text{Cu}_2\text{O}/\text{FePO}_4$ with anti-photocorrosion capability using a hydrothermal method.

Photodegradation, as a probe reaction, demonstrated that the CF spherical material exhibited superior photocatalytic performance compared to single Cu₂O and FePO₄. Characterization techniques such as BET, DRS, PL, photocurrent, and EIS confirmed that the CF1.5 nanocomposite material exhibited a larger specific surface area, enhanced visible light absorption capacity, and efficient electron–hole pair separation compared to single Cu₂O. These improvements were closely related to the establishment of the Z-scheme heterojunction. XPS analysis and cycling experiments revealed that the content of Cu(I) and catalytic activity did not significantly decrease, indicating that CF1.5 exhibited excellent anti-photocorrosion. Furthermore, free radical trapping experiments and ESR tests revealed that ·OH and ·O₂[−] radicals were the main active species in the photodegradation by CF1.5 photocatalyst. This study introduced a novel Z-scheme photocatalytic material CF1.5, which not only expands the application of Cu₂O in anti-photocorrosion materials but also contributes positively to mitigating environmental pollution issues.

Supplementary Materials: The following supporting information can be downloaded at: <https://www.mdpi.com/article/10.3390/reactions6020024/s1>, Figure S1: SEM image of Cu₂O/1.5Na₂HPO₄. Figure S2: SEM image of Cu₂O/1.5Fe(NO₃)₃·9H₂O. Figure S3: SEM image of CF0.5. Figure S4: SEM image of CF. Figure S5: SEM image of CF2. Figure S6: XPS analysis of as-prepared CF1.5 of P 2p. Table S1: The atomic percentage content of CF1.5. Table S2: Recent work on the degradation of MB by Cu₂O based photocatalysts [58–63].

Author Contributions: Conceptualization, K.Z. and Y.Z.; methodology, K.Z.; software, K.Z., F.C. and H.Q.; validation, X.Z., L.C., B.W., X.Y., H.Z. (Haonan Zou), B.L. and Y.H.; formal analysis, K.Z., L.Z. and Y.Z.; investigation, K.Z.; resources, H.Z. (Haonan Zou) and Y.Z.; data curation, K.Z.; writing—original draft preparation, K.Z.; writing—review and editing, K.Z., L.Z. and Y.Z.; visualization, K.Z. and Y.Z.; supervision, T.M., Y.Z. and H.Z. (Hu Zhou); project administration, H.Z. (Hu Zhou); funding acquisition, Y.Z. and H.Z. (Hu Zhou). All authors have read and agreed to the published version of the manuscript.

Funding: This research was funded by the Science and Technology Innovation Program of Hunan Province (Grant No. 2023RC1069) and Hunan Provincial Department of Education Outstanding Youth Fund Project (23B0498).

Data Availability Statement: The original contributions presented in this study are included in the article/Supplementary Material. Further inquiries can be directed to the corresponding author(s).

Acknowledgments: Thanks to everyone who contributed to this article.

Conflicts of Interest: The authors declare no conflicts of interest.

Abbreviations

The following abbreviations are used in this manuscript:

CF	Cu ₂ O/FePO ₄
MB	methylene blue
CR	Congo red
TC	tetracycline

References

1. Kou, T.; Wang, Y.; Zhang, C.; Sun, J.; Zhang, Z. Adsorption behavior of methyl orange onto nanoporous core–shell Cu@Cu₂O nanocomposite. *Chem. Eng. J.* **2013**, *223*, 76–83. [\[CrossRef\]](#)
2. Jiang, D.; Xue, J.; Wu, L.; Zhou, W.; Zhang, Y.; Li, X. Photocatalytic performance enhancement of CuO/Cu₂O heterostructures for photodegradation of organic dyes: Effects of CuO morphology. *Appl. Catal. B Environ.* **2017**, *211*, 199–204. [\[CrossRef\]](#)
3. Huang, C.; Long, Z.; Miyauchi, M.; Qiu, X. A facile one-pot synthesis of Cu–Cu₂O concave cube hybrid architectures. *CrystEng-Comm* **2014**, *16*, 4967–4972. [\[CrossRef\]](#)

4. Schneider, J.; Matsuoka, M.; Takeuchi, M.; Zhang, J.; Horiuchi, Y.; Anpo, M.; Bahnemann, D.W. Understanding TiO₂ Photocatalysis: Mechanisms and Materials. *Chem. Rev.* **2014**, *114*, 9919–9986. [\[CrossRef\]](#)
5. Liao, B.; Gao, J.; Weng, P.; He, L.; Zhang, Y.; Liu, Q.; Zhou, Z. Semiconductor Effect from Pd(II) Porphyrin Metal to Its Ligand in Photocatalytic N-Dealkylation. *ChemSusChem* **2024**, *18*, e202401381. [\[CrossRef\]](#) [\[PubMed\]](#)
6. Zheng, X.-J.; Li, C.-L.; Zhao, M.; Zheng, Z.; Wei, L.-F.; Chen, F.-H.; Li, X.-L. Photocatalytic degradation of butyric acid over Cu₂O/Bi₂WO₆ composites for simultaneous production of alkanes and hydrogen gas under UV irradiation. *Int. J. Hydrogen Energy* **2017**, *42*, 7917–7929. [\[CrossRef\]](#)
7. Zhang, F.; Dong, G.; Wang, M.; Zeng, Y.; Wang, C. Efficient removal of methyl orange using Cu₂O as a dual function catalyst. *Appl. Surf. Sci.* **2018**, *444*, 559–568. [\[CrossRef\]](#)
8. Nwanya, A.C.; Razanamahandry, L.C.; Bashir, A.; Ikpo, C.O.; Nwanya, S.C.; Botha, S.; Ntwampe, S.; Ezema, F.I.; Iwuoha, E.I.; Maaza, M. Industrial textile effluent treatment and antibacterial effectiveness of Zea mays L. Dry husk mediated bio-synthesized copper oxide nanoparticles. *J. Hazard. Mater.* **2019**, *375*, 281–289. [\[CrossRef\]](#)
9. Kwon, Y.; Soon, A.; Han, H.; Lee, H. Shape effects of cuprous oxide particles on stability in water and photocatalytic water splitting. *J. Mater. Chem. A* **2014**, *3*, 156–162. [\[CrossRef\]](#)
10. Toe, C.Y.; Zheng, Z.; Wu, H.; Scott, J.; Amal, R.; Ng, Y.H. Photocorrosion of cuprous oxide in hydrogen production: Rationalising self-oxidation or self-reduction. *Angew. Chem. Int. Edit.* **2018**, *57*, 13613–13617. [\[CrossRef\]](#)
11. Xiong, L.; Xiao, H.; Chen, S.; Chen, Z.; Yi, X.; Wen, S.; Zheng, G.; Ding, Y.; Yu, H. Fast and simplified synthesis of cuprous oxide nanoparticles: Annealing studies and photocatalytic activity. *RSC Adv.* **2014**, *4*, 62115–62122. [\[CrossRef\]](#)
12. Xu, W.; Jia, J.; Wang, T.; Li, C.; He, B.; Zong, J.; Wang, Y.; Fan, H.J.; Xu, H.; Feng, Y.; et al. Continuous tuning of Au–Cu₂O janus nanostructures for efficient charge separation. *Angew. Chem.* **2020**, *132*, 22430–22435. [\[CrossRef\]](#)
13. Lu, B.; Liu, A.; Wu, H.; Shen, Q.; Zhao, T.; Wang, J. Hollow Au–Cu₂O core–shell nanoparticles with geometry-dependent optical properties as efficient plasmonic photocatalysts under visible LIGHT. *Langmuir* **2016**, *32*, 3085–3094. [\[CrossRef\]](#) [\[PubMed\]](#)
14. Nie, J.; Yu, X.; Liu, Z.; Wei, Y.; Zhang, J.; Zhao, N.; Yu, Z.; Yao, B. Boosting principles for the photocatalytic performance of Cr-doped Cu₂O crystallites and mechanisms of photocatalytic oxidation for levofloxacin. *Appl. Surf. Sci.* **2022**, *576*, 151842. [\[CrossRef\]](#)
15. Liu, Z.; Yu, X.; Yang, F.; Wang, K.; Zhang, J.; Zhao, N.; Chen, L.; Niu, J. Synthesis of Co-doped Cu₂O Particles and Evaluation of their Photocatalytic Activity in the Degradation of Norfloxacin. *ChemistrySelect* **2022**, *7*, e202203682. [\[CrossRef\]](#)
16. Nie, J.; Yu, X.; Liu, Z.; Zhang, J.; Ma, Y.; Chen, Y.; Ji, Q.; Zhao, N.; Chang, Z. Energy band reconstruction mechanism of Cl-doped Cu₂O and photocatalytic degradation pathway for levofloxacin. *J. Clean. Prod.* **2022**, *363*, 132593. [\[CrossRef\]](#)
17. Zhang, L.; Meng, Y.; Xie, B.; Ni, Z.; Xia, S. Br doping promotes the transform of Cu₂O (100) to Cu₂O (111) and facilitates efficient photocatalytic degradation of tetracycline. *Mol. Catal.* **2023**, *548*, 113431. [\[CrossRef\]](#)
18. Bai, W.; Wu, M.; Du, X.; Gong, W.; Ding, Y.; Song, C.; Liu, L. Synergistic effect of multiple-phase rGO/CuO/Cu₂O heterostructures for boosting photocatalytic activity and durability. *Appl. Surf. Sci.* **2021**, *544*, 148607. [\[CrossRef\]](#)
19. Huang, W.-C.; Lyu, L.-M.; Yang, Y.-C.; Huang, M.H. Synthesis of Cu₂O Nanocrystals from Cubic to Rhombic Dodecahedral Structures and Their Comparative Photocatalytic Activity. *J. Am. Chem. Soc.* **2011**, *134*, 1261–1267. [\[CrossRef\]](#)
20. Zhang, L.; Shi, J.; Liu, M.; Jing, D.; Guo, L. Photocatalytic reforming of glucose under visible light over morphology controlled Cu₂O: Efficient charge separation by crystal facet engineering. *Chem. Commun.* **2014**, *50*, 192–194. [\[CrossRef\]](#)
21. Zhang, Y.; Zhang, Z.; Zhang, Y.; Li, Y.; Yuan, Y. Shape-dependent synthesis and photocatalytic degradation by Cu₂O nanocrystals: Kinetics and photocatalytic mechanism. *J. Colloid Interface Sci.* **2023**, *651*, 117–127. [\[CrossRef\]](#) [\[PubMed\]](#)
22. Feng, L.; Zhang, C.; Gao, G.; Cui, D. Facile synthesis of hollow Cu₂O octahedral and spherical nanocrystals and their morphology-dependent photocatalytic properties. *Nanoscale Res. Lett.* **2012**, *7*, 276. [\[CrossRef\]](#)
23. Tang, H.; Liu, X.; Xiao, M.; Huang, Z.; Tan, X. Effect of particle size and morphology on surface thermodynamics and photocatalytic thermodynamics of nano-Cu₂O. *J. Environ. Chem. Eng.* **2017**, *5*, 4447–4453. [\[CrossRef\]](#)
24. Rabbani, A.W.; Naz, G.; Berdimurodov, E.; Lal, B.; Sailauovna, A.B.; Bandegharai, A.H. Visible-light-driven photocatalytic properties of copper(I) oxide (Cu₂O) and its graphene-based NANOCOMPOSITES. *Baghdad Sci. J.* **2023**, *20*, 1064. [\[CrossRef\]](#)
25. Zhang, Y.-H.; Liu, M.-M.; Chen, J.-L.; Fang, S.-M.; Zhou, P.-P. Recent advances in Cu₂O-based composites for photocatalysis: A review. *Dalton Trans.* **2021**, *50*, 4091–4111. [\[CrossRef\]](#)
26. Yu, X.; Li, Z.; Liu, Z.; Wang, K. Fabrication of p–n Cu₂O/CaWO₄ heterojunctions for the efficient degradation of tetracycline and doxycycline. *Appl. Surf. Sci.* **2024**, *665*, 160285. [\[CrossRef\]](#)
27. Ke, J.; Zhao, C.; Zhou, H.; Duan, X.; Wang, S. Enhanced solar light driven activity of p–n heterojunction for water oxidation induced by deposition of Cu₂O on Bi₂O₃ microplates. *Sustain. Mater. Technol.* **2019**, *19*, e00088. [\[CrossRef\]](#)
28. Sun, K.; Zhao, X.; Zhang, Y.; Wu, D.; Zhou, X.; Xie, F.; Tang, Z.; Wang, X. Enhanced photocarrier separation in novel Z-scheme Cu₂ZnSnS₄/Cu₂O heterojunction for excellent photocatalyst hydrogen generation. *Mater. Chem. Phys.* **2020**, *251*, 123172. [\[CrossRef\]](#)

29. Bi, Z.-X.; Guo, R.-T.; Hu, X.; Wang, J.; Chen, X.; Pan, W.-G. Fabrication of a concave cubic Z-scheme $\text{ZnIn}_2\text{S}_4/\text{Cu}_2\text{O}$ heterojunction with superior light-driven CO_2 reduction Performance. *Energy Fuels* **2023**, *37*, 6036–6048. [\[CrossRef\]](#)
30. Zhang, Y.; Lu, S.-Y.; Shi, Z.; Zhao, Z.L.; Liu, Q.; Gao, J.-C.; Liang, T.; Zou, Z.; Li, C.M. A multi-component $\text{Cu}_2\text{O}@ \text{FePO}_4$ core–cage structure to jointly promote fast electron transfer toward the highly sensitive in situ detection of nitric oxide. *Nanoscale* **2019**, *11*, 4471–4477. [\[CrossRef\]](#)
31. Lou, S.; Wang, W.; Wang, L.; Zhou, S. In-situ oxidation synthesis of $\text{Cu}_2\text{O}/\text{Ag}/\text{AgCl}$ microcubes with enhanced visible-light photocatalytic activity. *J. Alloys Compd.* **2019**, *781*, 508–514. [\[CrossRef\]](#)
32. Beshkar, F.; Al-Nayili, A.; Amiri, O.; Salavati-Niasari, M.; Mousavi-Kamazani, M. Visible light-induced degradation of amoxicillin antibiotic by novel CuI/FePO_4 p-n heterojunction photocatalyst and photodegradation mechanism. *J. Alloys Compd.* **2022**, *892*, 162176. [\[CrossRef\]](#)
33. Zhou, H.; Yue, X.; Lv, H.; Kong, L.; Ji, Z.; Shen, X. Graphene oxide- FePO_4 nanocomposite: Synthesis, characterization and photocatalytic properties as a Fenton-like catalyst. *Ceram. Int.* **2018**, *44*, 7240–7244. [\[CrossRef\]](#)
34. Altaee, H.; Alshamsi, H.A. Selective oxidation of benzyl alcohol by reduced graphene oxide supported platinum nanoparticles. *J. Phys. Conf. Ser.* **2020**, *1664*, 012074. [\[CrossRef\]](#)
35. Mimouni, I.; Yahya, M.; Bouziani, A.; Naciri, Y.; Maarouf, F.-E.; El Belghiti, M.A.; El Azzouzi, M. Iron phosphate for photocatalytic removal of Ibuprofen from aqueous media under sun-like irradiation. *J. Photochem. Photobiol. A Chem.* **2022**, *433*, 114170. [\[CrossRef\]](#)
36. Tuo, X.-J.; Ye, Q.-L.; Wang, J.-L.; Chang, Y.; Zha, F. Study on Photocatalytic Properties of $\text{g-C}_3\text{N}_4/\text{FePO}_4$ Nanocomposites Under Visible Light. *Arab. J. Sci. Eng.* **2018**, *43*, 3541–3546. [\[CrossRef\]](#)
37. Atuchin, V.; Subanakov, A.; Aleksandrovsky, A.; Bazarov, B.; Bazarova, J.; Dorzhieva, S.; Gavrilova, T.; Krylov, A.; Molokeev, M.; Oreshonkov, A.; et al. Exploration of structural, thermal, vibrational and spectroscopic properties of new noncentrosymmetric double borate $\text{Rb}_3\text{NdB}_6\text{O}_{12}$. *Adv. Powder Technol.* **2017**, *28*, 1309–1315. [\[CrossRef\]](#)
38. Atuchin, V.; Isaenko, L.; Kesler, V.; Lin, Z.; Molokeev, M.; Yelissev, A.; Zhurkov, S. Exploration on anion ordering, optical properties and electronic structure in $\text{K}_3\text{WO}_3\text{F}_3$ elpasolite. *J. Solid State Chem.* **2012**, *187*, 159–164. [\[CrossRef\]](#)
39. Wang, H.; Quan, X.; Xiong, Q.; Yin, L.; Tian, Y.; Zhang, J. Enhanced performance of β -cyclodextrin modified Cu_2O nanocomposite for efficient removal of tetracycline and dyes: Synergistic role of adsorption and photocatalysis. *Appl. Surf. Sci.* **2023**, *621*, 156735. [\[CrossRef\]](#)
40. Wang, S.; Zhang, D.; Zhang, D.; Pu, X.; Liu, J.; Li, H.; Cai, P. A novel hydrangea-like $\text{ZnIn}_2\text{S}_4/\text{FePO}_4$ S-scheme heterojunction via internal electric field for boosted photocatalytic H_2 evolution. *J. Alloys Compd.* **2023**, *967*, 171862. [\[CrossRef\]](#)
41. Yu, L.; Ba, X.; Qiu, M.; Li, Y.; Shuai, L.; Zhang, W.; Ren, Z.; Yu, Y. Visible-light driven CO_2 reduction coupled with water oxidation on Cl-doped Cu_2O nanorods. *Nano Energy* **2019**, *60*, 576–582. [\[CrossRef\]](#)
42. Liao, H.; Wang, Z. Adsorption removal of amaranth by nanoparticles-composed Cu_2O microspheres. *J. Alloys Compd.* **2018**, *769*, 1088–1095. [\[CrossRef\]](#)
43. Shu, J.; Wang, Z.; Huang, Y.; Huang, N.; Ren, C.; Zhang, W. Adsorption removal of Congo red from aqueous solution by polyhedral Cu_2O nanoparticles: Kinetics, isotherms, thermodynamics and mechanism analysis. *J. Alloys Compd.* **2015**, *633*, 338–346. [\[CrossRef\]](#)
44. Sehrawat, P.; Rana, S.; Mehta, S.K.; Kansal, S.K. Optimal synthesis of $\text{MoS}_2/\text{Cu}_2\text{O}$ nanocomposite to enhance photocatalytic performance towards indigo carmine dye degradation. *Appl. Surf. Sci.* **2022**, *604*, 154482. [\[CrossRef\]](#)
45. Liu, Z.; Nie, H.; Kong, B.; Xu, X.; He, F.; Wang, W. Enhanced visible-light photocatalytic activity of $\text{BiOBr}/\text{BiOCl}$ heterojunctions: A hybrid density functional investigation on the key roles of crystal facet and I-doping. *Int. J. Hydrogen Energy* **2023**, *51*, 733–747. [\[CrossRef\]](#)
46. Zeng, L.; Li, X.; Shi, Y.; Qi, Y.; Huang, D.; Tadé, M.; Wang, S.; Liu, S. FePO_4 based single chamber air-cathode microbial fuel cell for online monitoring levofloxacin. *Biosens. Bioelectron.* **2017**, *91*, 367–373. [\[CrossRef\]](#) [\[PubMed\]](#)
47. Chen, C.; Chen, Q.; Li, Y.; Yang, J.; Huang, B.; Liu, X.; Xing, X.; Xiao, S.; Chen, S.; Wang, R. Microspherical $\text{LiFePO}_{3.98}\text{F}_{0.02}/3\text{DG}/\text{C}$ as an advanced cathode material for high-energy lithium-ion battery with a superior rate capability and long-term cyclability. *Ionics* **2020**, *27*, 1–11. [\[CrossRef\]](#)
48. Wang, Y.; Lei, H.; Lu, S.; Yang, Z.; Bin Xu, B.; Xing, L.; Liu, T.X. Cu_2O nano-flowers/graphene enabled scaffolding structure catalyst layer for enhanced CO_2 electrochemical reduction. *Appl. Catal. B: Environ.* **2022**, *305*, 121022. [\[CrossRef\]](#)
49. Wu, J.; Huang, P.; Fan, H.; Wang, G.; Liu, W. Metal–Organic Framework-Derived p- $\text{Cu}_2\text{O}/\text{n-Ce-Fe}_2\text{O}_3$ Heterojunction Nanorod Photoanode Coupling with a FeOOH Cocatalyst for High-Performance Photoelectrochemical Water Oxidation. *ACS Appl. Mater. Interfaces* **2020**, *12*, 30304–30312. [\[CrossRef\]](#)
50. Teo, J.J.; Chang, Y.; Zeng, H.C. Fabrications of hollow nanocubes of Cu_2O and Cu via reductive self-assembly of CuO nanocrystals. *Langmuir* **2006**, *22*, 7369–7377. [\[CrossRef\]](#)
51. Wang, L.; Cheng, B.; Zhang, L.; Yu, J. In situ irradiated XPS investigation on S-scheme $\text{TiO}_2@ \text{ZnIn}_2\text{S}_4$ photocatalyst for efficient photocatalytic CO_2 reduction. *Small* **2021**, *17*, 2103447. [\[CrossRef\]](#) [\[PubMed\]](#)

52. Zhang, P.; Li, Y.; Zhang, Y.; Hou, R.; Zhang, X.; Xue, C.; Wang, S.; Zhu, B.; Li, N.; Shao, G. Photogenerated Electron Transfer Process in Heterojunctions: In Situ Irradiation XPS. *Small Methods* **2020**, *4*, 2000214. [\[CrossRef\]](#)
53. Low, J.; Dai, B.; Tong, T.; Jiang, C.; Yu, J. In Situ Irradiated X-Ray Photoelectron Spectroscopy Investigation on a Direct Z-Scheme TiO₂/CdS Composite Film Photocatalyst. *Adv. Mater.* **2018**, *31*, e1802981. [\[CrossRef\]](#)
54. Wu, P.; Peng, H.; Wu, Y.; Li, L.; Hao, X.; Peng, B.; Meng, G.; Wu, J.; Liu, Z. A Green Strategy to Synthesize Ag/Ag₃PO₄/Chitosan Composite Photocatalysts and Their Photocatalytic Degradation Performance Under Visible-Light Irradiation. *J. Electron. Sci. Technol.* **2020**, *18*, 13. [\[CrossRef\]](#)
55. Dong, K.; He, J.; Liu, J.; Li, F.; Yu, L.; Zhang, Y.; Zhou, X.; Ma, H. Photocatalytic performance of Cu₂O-loaded TiO₂/rGO nanoheterojunctions obtained by UV reduction. *J. Mater. Sci.* **2017**, *52*, 6754–6766. [\[CrossRef\]](#)
56. Choi, J.; Oh, H.; Han, S.-W.; Ahn, S.; Noh, J.; Park, J.B. Preparation and characterization of graphene oxide supported Cu, Cu₂O, and CuO nanocomposites and their high photocatalytic activity for organic dye molecule. *Curr. Appl. Phys.* **2017**, *17*, 137–145. [\[CrossRef\]](#)
57. Chen, L.; Yang, J.; Zeng, X.; Zhang, L.; Yuan, W. Adsorption of methylene blue in water by reduced graphene oxide: Effect of functional groups. *Mater. Express* **2013**, *3*, 281–290. [\[CrossRef\]](#)
58. Feng, H.; Zhang, Y.; Cui, F. Enhanced photocatalytic activity of Cu₂O for visible light-driven dye degradation by carbon quantum dots. *Environ. Sci. Pollut. R.* **2022**, *29*, 8613–8622. [\[CrossRef\]](#) [\[PubMed\]](#)
59. Alorabi, A.Q.; Hassan, M.S.; Algethami, J.S.; Baghdadi, N.E. Synthesis and characterization of Ag-AgVO₃/Cu₂O heterostructure with improved visible-light photocatalytic performance. *Sci. Progress.* **2021**, *4*, 00368504211050300. [\[CrossRef\]](#)
60. Surikanti, G.R.; Bajaj, P.; Sunkara, M.V. g-C₃N₄-mediated synthesis of Cu₂O To obtain porous composites with improved visible light photocatalytic degradation of organic dyes. *ACS. Omega.* **2019**, *4*, 17301–17316. [\[CrossRef\]](#)
61. Tian, L.; Rui, Y.; Sun, K.; Cui, W.; An, W. Surface decoration of ZnWO₄ nanorods with Cu₂O nanoparticles to build heterostructure with enhanced photocatalysis. *Nanomater.* **2018**, *8*, 33. [\[CrossRef\]](#)
62. Yu, X.; Zheng, X.; Wei, Y.; Wang, J.; Zhao, N.; Yang, Q.; Yu, Z.; Niu, J. Preparation of novel Cu/Cu₂O composite thin films by pulse deposition method and their enhanced photocatalytic performance for methylene blue. *J. Electrochem. Soc.* **2022**, *169*, 072505. [\[CrossRef\]](#)
63. Norouzi, A.; Nezamzadeh-Ejehieh, A. Investigation of the simultaneous interactions of experimental variables and mechanism pathway in the photodegradation of methylene blue by binary ZnO/Cu₂O photocatalyst. *Mater. Res. Bull.* **2023**, *164*, 112237. [\[CrossRef\]](#)

Disclaimer/Publisher’s Note: The statements, opinions and data contained in all publications are solely those of the individual author(s) and contributor(s) and not of MDPI and/or the editor(s). MDPI and/or the editor(s) disclaim responsibility for any injury to people or property resulting from any ideas, methods, instructions or products referred to in the content.